Annual energy yield of mono- and bifacial silicon heterojunction solar modules with high-index dielectric nanodisk arrays as anti-reflective and light trapping structures

EVGENIIA SLIVINA,[1,*] **DERK BÄTZNER,**[2] **RAPHAEL SCHMAGER,**[3] **MALTE LANGENHORST,**[3] **JONATHAN LEHR,**[4] **ULRICH W. PAETZOLD,**[3,4] **ULI LEMMER,**[4] **AND CARSTEN ROCKSTUHL**[1,5]

[1]*Institute of Theoretical Solid State Physics, Karlsruhe Institute of Technology, Wolfgang-Gaede-Str. 1, 76131, Karlsruhe, Germany*
[2]*Meyer Burger Research AG, Rouges-Terres 61, 2068 Hauterive, Switzerland*
[3]*Institute of Microstructure Technology, Karlsruhe Institute of Technology, Hermann-von-Helmholtz-Platz 1, 76344 Eggenstein-Leopoldshafen, Germany*
[4]*Light Technology Institute, Karlsruhe Institute of Technology, Engesserstrasse 13, 76131 Karlsruhe, Germany*
[5]*Institute of Nanotechnology, Karlsruhe Institute of Technology, Hermann-von-Helmholtz-Platz, 76344 Eggenstein-Leopoldshafen, Germany*
evgeniia.slivina@kit.edu

Abstract: While various nanophotonic structures applicable to relatively thin crystalline silicon-based solar cells were proposed to ensure effective light in-coupling and light trapping in the absorber, it is of great importance to evaluate their performance on the solar module level under realistic irradiation conditions. Here, we analyze the annual energy yield of relatively thin (crystalline silicon (c-Si) wafer thickness between 5 μm and 80 μm) heterojunction (HJT) solar module architectures when optimized anti-reflective and light trapping titanium dioxide (TiO$_2$) nanodisk square arrays are applied on the front and rear cell interfaces, respectively. Our numerical study shows that upon reducing c-Si wafer thickness down to 5 μm, the relative increase of the annual energy yield can go up to 23.3 %$_{rel}$ and 43.0 %$_{rel}$ for mono- and bifacial solar modules, respectively, when compared to the reference modules with flat optimized anti-reflective coatings of HJT solar cells.

1. Introduction

Reducing optical losses is of paramount importance for further developing photovoltaic (PV) devices. Even though the record efficiency for the silicon-based cells is quite close to the theoretical limit [1], further reduction of the optical losses can allow the market-dominating single-junction c-Si solar cells to reach their efficiency limit [2,3]. While a common approach involves employing various uniform anti-reflective coatings (ARCs) combined with the chemical texturing of the c-Si wafer, resulting in the formation of micron-sized pyramidal features [4], in some cases, alternative approaches to suppress the optical losses are of interest. Even though the small pyramidal textures for thin c-Si wafers are actively researched [5–7], in industrial solar cells, the micron-sized textures are realized on relatively thick c-Si wafers, with a current standard of 160 μm. However, a transition to the wafer thickness below the standard value and switching to the foil-like thinner c-Si can allow for lower material consumption. This can reduce the manufacturing cost and accelerate the expansion of PV manufacturing [8] to keep up with the estimates for the global installed PV capacity [9]. However, for such thin devices, the use of

micron-sized textures becomes very challenging due to c-Si wafer handling issues, and novel approaches have to be identified to reduce the optical losses.

In response to this need, various nanophotonic concepts [10] applicable to c-Si-based solar cell stacks were proposed to enhance light harvesting through improved light in-coupling on the front surface. Examples of possible solutions include plasmonic structures [11–13], periodically arranged silicon [14,15] and dielectric [16–18] nanoscatterers, and biomimetic structures [19]. Moreover, double-sided AR and light trapping (LT) nanostructure gratings introduced at the front and rear sides of the solar cells were also suggested. For example, such a concept was investigated for thin-film c-Si [20] and thin-film hydrogenated nanocrystalline silicon (nc-Si:H) [21] solar cells.

Nevertheless, while a plethora of nanophotonic structures was proposed and investigated in recent years, it is of paramount importance to analyze their performance in a full solar module architecture under realistic irradiation conditions. For example, such analysis was performed for different solar module architectures where sufficient optical properties were achieved using strategies involving textured interfaces and/or flat ARCs [22–27]. Since the solar cell is not always illuminated with light at normal incidence in the realistic scenario, one has to go beyond the analysis of the ability of the structure to enhance the short-circuit current density under the standard test conditions and ensure that the proposed AR and/or LT nanostructure designs are robust concerning irradiation impinging on the solar module at increasing angles of incidence. Additionally, the absorption of photons by the solar cell absorber depends on the sun's position. It is influenced by the cloud coverage effect on irradiation received by the module and the module orientation. For solar cells with double-sided photonic nanostructures, it is also appealing to consider and assess the possible power output of the solar modules with nanostructured solar cells in the case of a bifacial module architecture. This module configuration allows for harvesting the photons that can be absorbed when the sunlight either hits the module from its back or is reflected from the ground and can be absorbed in the solar cell.

Here, we study the energy yield of relatively thin wafer-based c-Si solar modules, for which the solar cell stack is coated with double-sided nanostructure gratings. Suitably designed square arrays of dielectric high-index TiO_2 nanodisks are used as AR and LT photonic nanostructures. Their geometrical parameters are subject to optimization. Results are compared to the modules containing more traditional planar thin-film anti-reflective layers. We consider mono- and bifacial modules and introduce the nanodisk arrays on both the front and rear surfaces of the c-Si-based heterojunction (HJT) solar cell for either module configuration. Additionally, we compare the modules with AR and LT nanostructures with the state-of-the-art modules for which the c-Si wafers have random pyramidal texture. The nanodisk arrays are initially optimized at normal incident light by full-wave optical simulations concerning the short-circuit current density associated with the reflected portion of the light (details in Sec. 2.4). The optimal design of these nanodisk arrays depends on whether they are employed on the front side, where they serve the purpose of suppressing reflectance, or on the rear side, where they facilitate the light trapping. Therefore, when optimizing the nanodisk arrays, different designs are found depending on the mechanisms through which they contribute to enhancing absorptance in the c-Si wafer. To estimate the annual energy yield (EY) of the solar module architectures with nanodisk arrays, the optical response from the optimized nanodisk arrays when placed on the front and rear solar cell contact layers is simulated using full-wave optical tools depending on the angle of incidence. This is the primary information fueled afterward into the EY modeling framework. The annual EY is assessed for monofacial and bifacial module architectures with and without TiO_2 nanodisk arrays at locations with different climate conditions. The influence of albedo radiation is also considered, which is especially relevant to consider in bifacial module configuration [28]. Our key contribution is to show that for the wafer-based c-Si cells with thicknesses for which standard chemical texturing becomes impractical, and alternative AR and LT structures are of interest, the

nanodisk arrays that we suggest outperform to a considerable extent the traditional design that relies only on the planar ARCs and approach the performance of the random pyramidal textures. In passing, we note that the design of the nanodisk arrays for front and rear solar cell contacts proposed here is exemplary, and it is neither restricted to a particular solar cell stack nor the materials used.

2. Module architectures and numerical methods

2.1. Investigated module architectures and material properties

The six different architectures discussed in this contribution are schematically depicted in Fig. 1. The extensive annual EY calculations were performed for two reference monofacial and bifacial module configurations with standard flat ARC (architectures (a) and (c)) and two designs with AR and LT nanodisk arrays introduced on top of the front and rear ITO contact layers (architectures (b) and (d)), respectively. We varied the c-Si absorber thickness of all architectures between $5\,\mu$m, and $80\,\mu$m, which is a typical thickness range between thin PV and conventional wafer-based c-Si PV. Additionally, we compared the performance of the modules with nanodisks to the performance of the state-of-the-art modules with random pyramidal texture (architectures (e) and (f)) for a few c-Si wafer thicknesses.
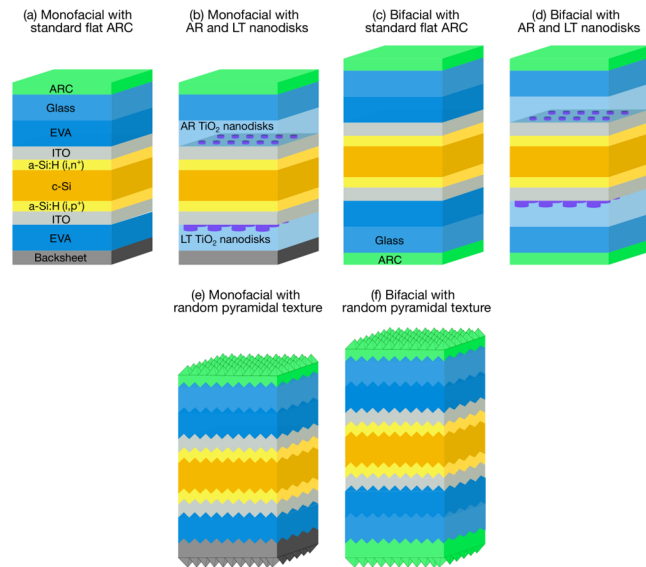
Fig. 1. Schematic representation of the six solar module architectures discussed in this paper: (a) Monofacial reference module with an optimized transparent conductive ITO layer on the front, serving as both ARC and front contact, and perfectly reflective backsheet in the rear of the module. Front ITO layer is preceded with window glass and encapsulation (EVA) layers covered with an ARC. The rear ITO layer is followed by the EVA layer identical to the one on the front of the architecture. For all considered solar module configurations, the window layers are identical. (b) Monofacial module with optimized AR and LT nanodisk arrays on top of the front and rear ITO contacts, respectively. The rear EVA layer is followed by the backsheet as in the reference architecture. (c) Bifacial reference module with the standard flat ARC with symmetric window layers on both sides of the solar module. (d) Bifacial module with optimized AR and LT nanodisk arrays on top of the front and rear ITO contacts with symmetric window layers on both sides of the solar module, respectively. (e) State-of-the-art monofacial module architecture with a chemically textured c-Si wafer. (f) State-of-the-art bifacial module architecture with a chemically textured c-Si wafer.

In the case of flat reference c-Si HJT solar cell stacks, the front hydrogenated amorphous silicon (a-Si:H) (passivation intrinsic and n$^+$ doped, the thickness can be found in [29]) and conducting ITO (75 nm) layers were considered. For the rear side of the HJT solar cell stack, the a-Si:H (passivation intrinsic and p$^+$ doped) layer was slightly thicker than the a-Si:H layer on the front, while the ITO layer was thinner than its counterpart on the front side.

The configurations (b) and (d) containing optimized AR nanodisk array had a reduced front ITO thickness of 10 nm with TiO$_2$ nanodisks arranged in a square lattice of 320 nm pitch, with individual nanodisk having a radius of 125 nm and a height of 90 nm. The design of the AR nanodisk array was based on the previous work on helicity preserving TiO$_2$ nanodisk array for the front interface of a c-Si HJT solar cell, where efficient and broadband backscattering suppression was achieved due to the ability of the system to suppress cross-talk between opposite helicities (handedness) of the electromagnetic field upon light-matter interaction [29]. The configurations (b) and (d) also had the optimized LT TiO$_2$ nanodisk square array (individual nanodisk with a radius of 215 nm and height of 395 nm, 565 nm pitch) while the rear ITO thickness was the same as for the reference architectures (a) and (c). These values for the geometrical parameters are the results of an optimization of the AR and LT nanodisk arrays discussed in Sec. 2.4.

For both monofacial and bifacial architectures, we considered the bifacial solar cells with identical contacting metallic grids on both sides of the cells. We note that the effect of the contacts on the optical performance of the solar modules was neglected. To mimic the performance of the perfectly reflective backsheet in the monofacial module architectures, we considered the 200 nm thick silver layer at the rear side of such modules. The window module layers comprise encapsulating EVA (400 μm) and glass (4 mm) with thin-film anti-reflective MgF$_2$ coating (130 nm). The modules in the bifacial configuration were considered to have the same window layers as the ones introduced on the front side. In such a configuration, the module can absorb the light that is incident on both its front and rear sides. Additionally, one can harvest albedo radiation since the transmitted portion of the light is reflected from the ground, and thus, can be reabsorbed in the silicon, significantly boosting the annual EY. When a bifacial solar module is tilted, albedo radiation can also impact the annual EY due to the light reflected from the ground and incident on the front of the module. We note that when a monofacial solar module is tilted, albedo radiation that is incident on the front of the module can also be considered.

Refractive indices of c-Si, TiO$_2$, ITO, and Ag used in the calculations were taken from literature [30–33]. Refractive index data for the front and rear composite (passivation intrinsic and doped) a-Si:H layers were obtained using ellipsometry, and corresponding *n* and *k* values provided by Meyer Burger Research AG are plotted in Fig. 2. For the window layers, a non-absorbing optically thick glass layer was considered to have a nondispersive refractive index of *n* = 1.5. We note that since the glass layer is non-absorbing, its thickness does not influence the performance of the solar modules. The refractive index data of EVA and MgF$_2$ were taken from [34] and [35], respectively. Although MgF$_2$ is not stable under outdoor conditions, we chose this material for the ARC on top of the window layers since we focus mainly on the optical properties of the investigated architectures, and MgF$_2$ can be easily included in our model.

2.2. Simulation framework

The numerical simulations of the EVA-cell interface for both AR and LT TiO$_2$ nanodisk arrays were performed using the finite element method (FEM) with commercial software *JCMsuite* [36]. The annual EY was calculated using a comprehensive modeling framework [37] enabling the quick simulation of various and sophisticated PV architectures under realistic irradiation conditions discussed in detail in [38].
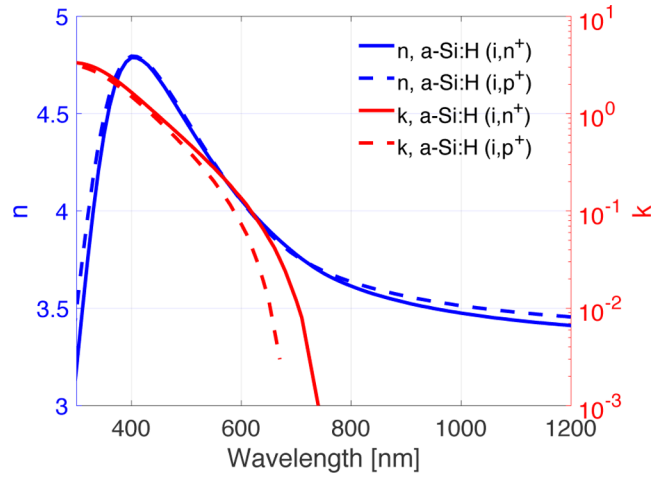
Fig. 2. Refractive index n and extinction coefficient k of a-Si:H composite layers. The measured data were fitted to a Tauc-Lorentz model.

2.3. Electrical parameters

The electrical parameters corresponding to a typical c-Si HJT solar cell used in the annual EY calculation are summarized in Table 1. The shadowing by electrical connections for all considered architectures is disregarded.

Table 1. Electrical parameters of the solar cell

Shunt resistance, R_{sh} [$\Omega \cdot cm^2$]	5000
Series resistance, R_s [$\Omega \cdot cm^2$]	0.7
Reverse-blocking current, J_0 [A/cm^2]	$2 \cdot 10^{-13}$
Ideality factor, n_{id}	1.1
Temperature coefficient of J_{SC}, $t_{J_{SC}}$ [%/K]	0.05
Temperature coefficient of V_{OC}, $t_{V_{OC}}$ [%/K]	−0.25

A device characterized by these properties would have a J_{SC} around 38.3 mA/cm^2. This yields $V_{OC} = 0.734$ V at temperature $T = 25°C$ from the following equation:

$$V_{OC} = n_{id} V_{th} \ln\left(\frac{J_{SC}}{J_0} + 1\right), \tag{1}$$

where the thermal voltage $V_{th} = kT/q = 0.0257$ V with k being the Boltzmann constant. The values of ideality factor and reverse-blocking current can be found in Table 1.

2.4. Calculation of reflectance, transmittance, and absorptance

At the EVA-cell interfaces with introduced AR and LT nanodisk arrays, reflectance and transmittance into all scattering directions at each wavelength and incidence polar and azimuth angles are calculated as the ratio of the scattered reflected or transmitted power to the power of the incident field. At the investigated interfaces, both c-Si and EVA are assumed to be semi-infinite. In general, when such semi-infinite substrate and supersaturate are considered, one has to keep in mind that the EVA-glass and glass-air interfaces can have an influence on the optical performance of the nanostructured system [39]. However, the wafer thicknesses we consider here lie in the region between the thin PV and conventional c-Si PV, leading to reduction of such an influence

on the optical response of the system. Moreover, the matrix formalism used in the EY modeling framework takes into account the light-matter interaction at the EVA-glass and glass-air interfaces and couples it with the nanocoated cell-EVA interface, calculating the matrix describing the optical response of the whole solar module stack. For a given azimuth angle ϕ_{in}, reflectance and transimittance values form matrices of the size ($N_{\theta_{in}}$, $N_{\theta_{r,t}}$, N_λ), where the entries correspond to all polar angles of incidence, scattering angles, and wavelengths, respectively. The polar angle θ_{in} is varied from 0° to 89° with 5° step, and the results are then interpolated at intervals of 1°. In case of azimuth angle ϕ_{in}, the symmetry of the nanodisk coating is exploited, and only calculations for angles between 0° and 45° with 15° step are performed. The calculated matrices for different ϕ_{in} values are subsequently averaged. Total reflectance and transmittance for a certain wavelength and incident polar and azimuth angles are calculated according to:

$$R = \frac{\sum_{\boldsymbol{k}_r} |\tilde{\boldsymbol{E}}(k_{r,x}, k_{r,y})|^2 \cdot \cos(\theta_r)}{|\boldsymbol{E}_0|^2 \cos(\theta_{in})}, \tag{2}$$

$$T = \frac{\sum_{\boldsymbol{k}_t} n_{out} |\tilde{\boldsymbol{E}}(k_{t,x}, k_{t,y})|^2 \cdot \cos(\theta_t)}{n_{in} |\boldsymbol{E}_0|^2 \cos(\theta_{in})}, \tag{3}$$

where $\boldsymbol{k}_{r,t}$ are the wave vectors of reflected and transmitted fields, $\theta_{r,t} = \mathfrak{R}(\pm k_z/k_{r,t})$ are the scattering angles, $\boldsymbol{E}_0$ is the amplitude of an incident plane wave with a mixed TE-TM polarization, and n_{in} and n_{out} are the refractive indices of the media where the incident and scattered waves propagate, respectively. We use the angular spectrum representation of the fields, and $\tilde{\boldsymbol{E}}(k_{\{r,t\},x}, k_{\{r,t\},y})$ in Eqs. (2) and (3) is calculated by means of the Fourier transform of the electric fields in real space obtained from full-wave simulations. Absorptance in each of the thin film layers and nanodisk array was calculated by integrating the divergence of the Poynting vector across the absorber volume, thus yielding absorbed power which is normalized to the power of the incident plane wave. Similarly to reflectance and transmittance, for a given azimuth angle, absorptance values form a matrix of the size (N_m, $N_{\theta_{in}}$, N_λ), where index m runs over all absorbing layers in the front or rear solar cell stack. The angular dependent simulations were performed for optimized AR and LT nanodisk arrays. The optical performance of the nanodisk arrays was optimized with respect to the short-circuit current density associated with reflectance at a normal light incidence, which is calculated using the following equation:

$$J_{SC,R} = \int_{\lambda_1}^{\lambda_2} e \frac{SI_{AM1.5}(\lambda)R(\lambda)}{E_{ph}} d\lambda, \tag{4}$$

where e is the electron charge, $E_{ph} = hc/\lambda$ is the energy of a photon, and $SI_{AM1.5}(\lambda)$ is the spectral irradiance. For this calculation, air mass 1.5 global (AM1.5G) tilted irradiance raw data was taken from [40], and the total reflectance $R(\lambda)$ was interpolated accordingly. We note that we assume the perfect charge carrier collection efficiency when calculating $J_{SC,R}$. The short-circuit current density due to reflectance was minimized for the front nanodisk array and maximized for the rear LT nanodisk array. The optimization process was done by varying one of the geometrical parameters while the others were fixed. With such a procedure we cycled through all the parameters and optimized them sequentially until the global minimum and maximum value of $J_{SC,R}$ corresponding to the front and rear cell-encapsulation interfaces have been found. Within the EY modeling framework, where the optical response of the entire architecture is computed, the light propagation in multi-layer thin-film stacks is treated coherently, for which the transfer matrix method is employed. When AR and LT nanodisk arrays are considered instead of those thin-film layers, the corresponding output matrices for reflectance, transmittance, and absorptance are integrated into the modeling framework. For thicker layers, such as the c-Si

substate of the cell and window layers of the module, the assumption of coherence breaks down. The Beer-Lambert law can describe the absorption of the light in those layers:

$$I(z, \lambda) = I_0 \cdot e^{-\alpha(\lambda)z}, \tag{5}$$

where I_0 is the initial intensity, α is the absorption coefficient of the considered medium, and z is the distance traveled in it.

3. Results and discussion

3.1. Optical performance of solar modules

First, we will closely look at the optical properties of the cell interfaces with the optimized AR and LT nanodisk arrays. Figure 3 shows reflectance at normal incidence of the EVA-cell interfaces for the front and rear HJT solar cell contacts with AR and LT nanodisk arrays. For both nanodisk arrays and illumination directions, reflectances of the corresponding reference flat interfaces are plotted for comparison. The graphs (a) and (b) in Fig. 3 correspond to the optical response of the front EVA-cell interface. In this case, the objective was to minimize short-circuit current density corresponding to reflectance $J_{SC,R}$ introduced in Eq. (4), which resulted in an AR nanodisk array with reflectance shown in Fig. 3(a).
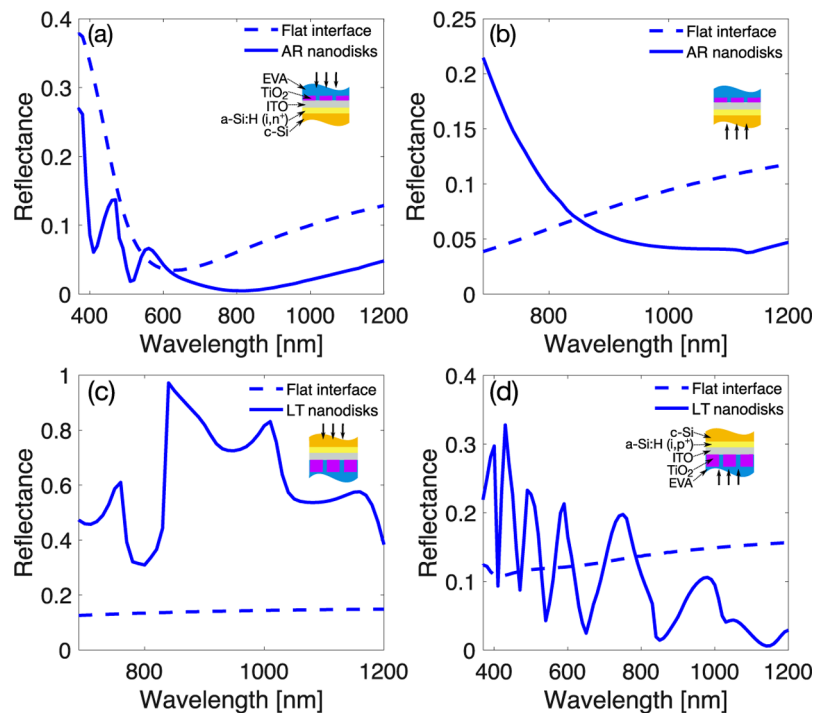
Fig. 3. Reflectance at normal incidence for the front and rear EVA-cell interfaces in case of both AR and LT nanodisk arrays. Inset sketches depict the corresponding interface and illumination direction. Interfaces are the same for the pairs of graphs (a)-(b) and (c)-(d), respectively.

As was briefly discussed in Sec. 2.1, the design of the AR nanodisk coating is related to the ability of the system to avoid cross-talk between the opposite helicities of the electromagnetic field. The helicity operator Λ is defined as the projection of the angular momentum operator **P** onto the direction of the linear momentum operator **J**, and its eigenvalues ± 1 correspond to the

opposite handednesses of the circularly polarized light. In [29], we have shown for a similar solar cell stack that upon normally incident illumination with the light of certain handedness, all the light reflected along the specular direction will be strictly of the flipped helicity (handedness), and at the wavelengths where the scattering is minimal, the system achieves helicity preservation in all scattering directions. The requirement for a system to be helicity preserving is to possess a high enough degree of rotational symmetry ($n \geq 3$) along the illumination direction. For normal light incidence, for which the optimization of AR nanodisk array was performed, the illumination direction is along the symmetry axis of an individual nanodisk, which essentially means that $n \to \infty$ in this case. The resulting reflectance of the AR nanodisk array is lower than the one of the reference optimized flat ARC and exceeds it slightly only in the wavelength region around $\lambda = 600$ nm, for which standard ARC of the solar cell is typically optimized. However, as shown in Fig. 3(b), the LT properties of this nanodisk array are not as good as its AR properties. When the light is impinging from the c-Si absorber, only the long-wavelength response is relevant since the short-wavelength photons are absorbed before reaching this interface. This nanodisk coating transmits the light reflected from the rear of the stack particularly strongly at longer wavelengths and is not possessing better LT properties than the standard flat reference. This optical response confirms that the front nanodisk array contributes to the light harvesting of the considered solar module architectures mainly by its AR properties.

The graphs (c) and (d) in Fig. 3 demonstrate the optical response of the optimized LT nanodisk array. Here, the structure parameters strongly differ from those of the helicity preserving AR nanodisk array. The larger and more sparsely spaced LT nanodisks allow for improved harvesting of the long-wavelength photons reaching the rear of the solar cell. The impinging light is effectively scattered into multiple directions since many diffraction orders are allowed. Taking into account the absorption depth of c-Si, for the minimal considered absorber thickness of 5 μm, the photons that can reach the rear contact of the solar cell have wavelengths $\lambda \geq 690$ nm. The optimized reflectance of the LT nanodisk array for the spectral region of interest is shown in Fig. 3(c). Its LT performance exceeds that of the flat reference solar cell stack at all wavelengths. Nevertheless, as can be seen from Fig. 3(d), though this nanodisk array outperforms its flat reference counterpart in terms of AR properties in the longer wavelength range, overall, its main contribution to the improved absorption in c-Si, and, consequently, the annual EY of the solar module, is due to its superior LT properties. This way, when nanodisk arrays with decoupled AR and LT properties are present on both sides of the solar cell stack, one can achieve a solid overall solar module performance boost.

Another critical aspect of the solar module's optical performance is parasitic absorption. Here, all discussed results are for a selected median c-Si absorber thickness of 40 μm and at normal light incidence. Figures 4 and 5 show absorptance in all layers of the monofacial and bifacial module stacks, respectively, except for the glass layer, which was assumed to be non-absorbing. Additionally, absorptance of the rear a-Si:H layer in monofacial module configuration and of the rear and front a-Si:H layers in the bifacial module configuration for forward and backward illumination direction, respectively, was negligible, and, thus, it is not shown. Moreover, the LT TiO$_2$ nanodisk array does not introduce any parasitic absorption upon forward illumination since the light absorbed in these nanodisks has short wavelengths and does not reach the rear cell interface while it is absorbed in c-Si. Similarly, the AR TiO$_2$ nanodisk array in the bifacial module configuration does not introduce any parasitic absorption upon backward illumination. The short-circuit current densities indicated on the top of all graphs in Fig. 4 and Fig. 5 were calculated assuming AM1.5G spectrum using the modified Eq. (4) with absorptance of c-Si instead of reflectance.

In the case of the reference module with standard flat ARC (Fig. 4(a)), the front transparent conductive ITO layer serves as an ARC but also introduces some parasitic absorption. However, when the AR nanodisk array is introduced (Fig. 4(b)), ITO thickness for the optimized front
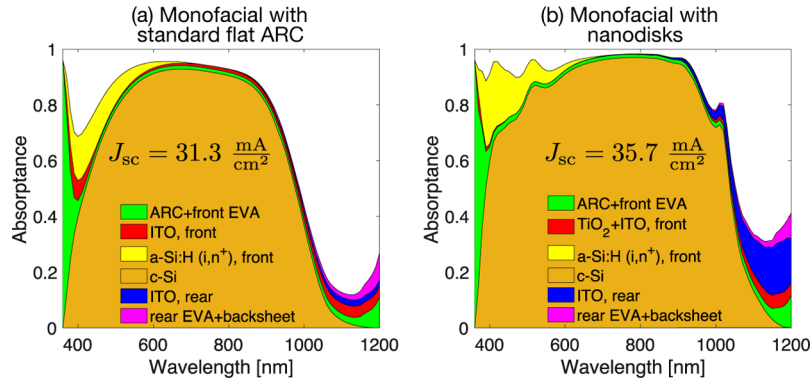
Fig. 4. Absorptance in the different layers of (a) the monofacial reference module with standard flat ARC and (b) the monofacial module with AR and LT nanodisk arrays on top of the front and rear ITO contacts at normal light incidence. For both solar module architectures, the c-Si absorber thickness was 40 μm.
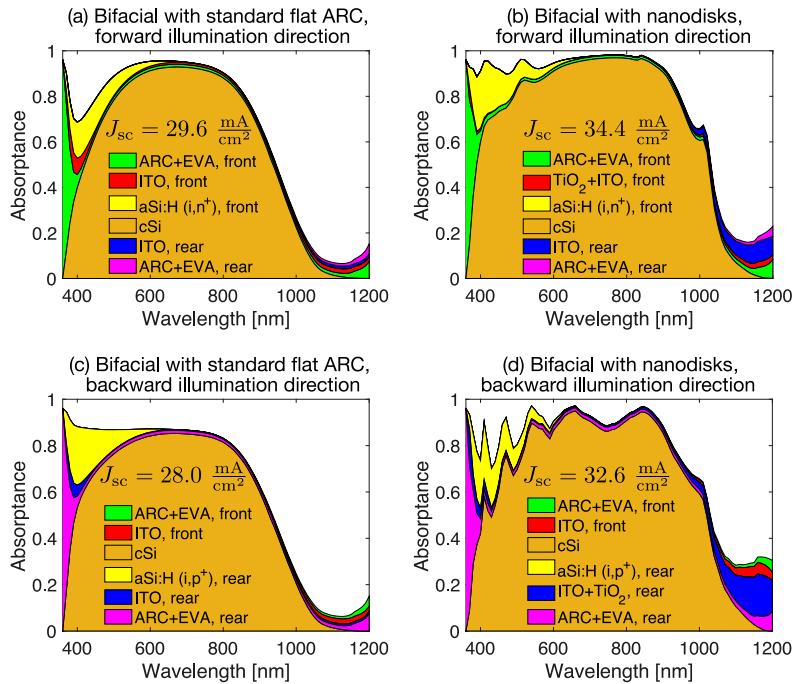
Fig. 5. Absorptance in the different layers of the bifacial solar modules at normal light incidence: (a) in case of forward illumination direction for the bifacial reference module with standard flat ARC, (b) in case of forward illumination direction for the bifacial module with AR and LT nanodisk coatings, (c) in case of backward illumination direction for the bifacial reference module with standard flat ARC, (d) in case of backward illumination direction for the bifacial module with AR and LT nanodisk coatings. For both solar module architectures, the c-Si absorber thickness was 40 μm.

solar cell contact is reduced considerably (from 75 to 10 nm), and parasitic absorption in this layer is significantly reduced. The nanodisks themselves have a tiny contribution to the parasitic absorption, considering that EVA absorbs all the light impinging on the solar module at the wavelengths between 300 and 360 nm and TiO_2 absorbs only at the wavelengths shorter than $\lambda = 380$ nm. On the other hand, while the AR nanodisk array increases absorptance in c-Si thanks to a better in-coupling of the incident light, it also increases parasitic absorption in the front a-Si:H layer. However, it should be noted that in [41] it was shown that the carriers which are absorbed in an intrinsic a-Si:H layer can still contribute to the short-circuit current, and thus the parasitic absorption loss in this layer represents an upper bound and can have a less of an impact in reality. The LT nanodisk array additionally boosts the optical performance improving absorptance in c-Si at the longer wavelengths. However, due to the strong scattering enabled by LT nanodisks, parasitic absorption is also increased for longer wavelengths. If we compare the short-circuit current density in the case of solar module architecture with the AR and LT nanodisk arrays to the short-circuit current density of the state-of-the-art architecture (Fig. 1(e)) for the same wafer thickness of 40 μm, the latter will have $J_{SC} = 36.1$ mA/cm^2, which yields the difference of 1.1 %$_{rel}$. Hence, although performing slightly worse than the random pyramidal texture, the nanodisk arrays allow for a broadband enhancement of absorptance in the silicon absorber layer and can provide a decent alternative to the pyramids in cases when the wafer texturing becomes tricky.

In the case of the bifacial standard reference module and forward illumination direction (Fig. 5(a)), the parasitic absorption for the wavelengths below $\lambda = 700$ nm is similar to the one of the monofacial module reference. However, the parasitic absorption is slightly lower in the long-wavelength range since more light is transmitted through the glass and encapsulation window layers. When AR and LT nanodisk arrays are introduced (Fig. 5(b)), they improve absorptance in silicon the same way as in the case of the monofacial module. When the light is impinging on the rear side of the bifacial solar module (Fig. 5(d)), absorptance in c-Si is also improved in the case when AR and LT arrays are introduced in comparison to the reference module with standard flat ARC (Fig. 5(c)), even though LT nanodisks are not optimal in terms of their AR properties and introduce dips in silicon absorptance due to the sharp spectral features which can be seen in Fig. 3(d). To compare with the state-of-the-art bifacial solar module architecture from Fig. 1(f), we once again look at the short-circuit current densities. For the bifacial module with the chemically textured 40 μm silicon wafer, J_{SC} in the case of forward and backward illumination directions were determined to be 34.7 mA/cm^2 and 34.6 mA/cm^2, respectively. Similar to the monofacial module architecture, the module with random pyramidal texture outperforms the module with the nanodisks, with the difference in J_{SC} being 0.9 %$_{rel}$ for the forward and 6.1 %$_{rel}$ for backward illumination direction.

3.2. *Energy yield of solar modules*

Having obtained the optical response of the systems with nanodisks at the front and rear cell-EVA interfaces, we analyzed the annual EY of the solar module architectures introduced in Fig. 1 for three cities in the United States of America located in different climate zones [42]. Two of the chosen cities, Anchorage, AK and Honolulu, HI, have highly contrasting irradiation conditions. The former is a cold and cloudy region (Boreal climate) and the latter a hot and sunny one (Tropical climate). The additionally chosen Kansas City, MO, has a temperate climate that receives an annual solar irradiance between Anchorage and Honolulu. By covering different climate zones, we aimed to highlight the robustness of the nanodisk arrays performance and their ability to improve the annual EY for all types of irradiation conditions, albeit with small differences that most likely originate from the spectral features introduced by the nanodisk arrays. The solar modules were considered to face south, and the tilt angles θ_m were optimized for each location. This resulted in θ_m values to be 38° for Anchorage, 30° for Kansas City, and 17°

for Honolulu, respectively. We note that the extensive annual EY analysis was performed for the module architectures (a)-(d) in Fig. 1. The annual EY of the architectures (e) and (f) was calculated only for one location (Kansas City) for a few select silicon wafer thicknesses.

Figure 6 demonstrates the relative improvement of the annual EY when the nanodisk arrays are used for light management instead of the optimized planar layers. The increase of the annual EY is shown as a function of the c-Si absorber thickness. For this calculation, no albedo was considered. In the realistic scenario, the bifacial solar modules are always installed on the surface with some albedo. However, the influence of albedo radiation on the EY is stronger for the sunnier locations. Thus, we assumed the absence of albedo to show the robustness of the performance of the solar modules with the nanocoated cell interfaces irrespective of the irradiation conditions. The relative increase of the annual EY reached up to 23.3 %$_{rel}$ and 43.0 %$_{rel}$ at the minimal wafer thickness of 5 μm for monofacial and bifacial architectures with nanodisks, respectively.
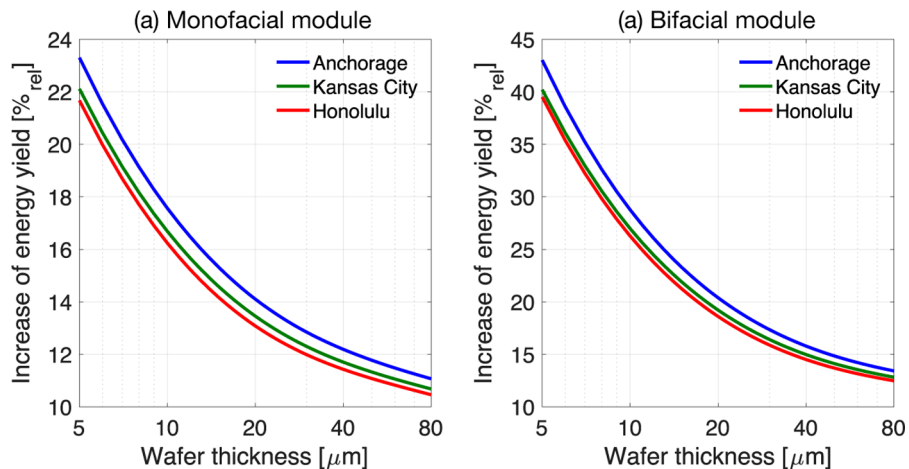
Fig. 6. Relative increase of the annual EY for three locations in case of (a) the monofacial solar module (comparing (b) to (a) from Fig. 1) and (b) the bifacial solar module (comparing (d) to (c) from Fig. 1) with varying thickness of the c-Si absorber.

As expected, for the monofacial case, the module with the AR and LT nanodisk arrays (Fig. 1(b)) outperforms the standard flat architecture with the optimized ARC (Fig. 1(a)), with this effect becoming even more apparent when reducing the c-Si absorber thickness. In the monofacial solar module case, the LT nanodisk array's sole purpose is to enhance the optical path length in the absorber. With the individual disk parameters being significantly larger when compared to the nanodisk array used as the AR structure at the front interface, the light which is not absorbed in the silicon and reaches the rear interface of the cell is effectively scattered in multiple directions, thus improving the LT properties of the cell. When instead of a reflective backsheet, the window encapsulation and glass layers are introduced (Fig. 1(d)) to take advantage of the solar irradiation which can hit the module on its back, the LT nanodisk array should also act as a decent ARC. From Fig. 6(b) it can be seen that it translates into an even more significant increase of the annual EY than for monofacial module architecture when comparing to a reference bifacial module architecture (Fig. 1(c)).

The comparison of the EY performance of the monofacial and bifacial architectures with nanodisks to the performance of the state-of-the-art architectures with random pyramidal textures is given in Table 2. We considered the two c-Si absorber thicknesses from the range we discuss in the paper – the median thickness of 40 μm, and the thickness of 80 μm below which the texturing of the wafer becomes complicated, and, finally, the standard thickness of c-Si wafer of 160 μm. In the case of the bifacial module architectures, we considered the sandstone ground surface.

Due to the differences between the short-circuit current densities for the modules with nanodisk arrays and random pyramidal texture discussed in Sec. 3.1, the state-of-the-art architectures outperform the architectures with the nanodisk arrays for all three wafer thicknesses. As expected, the minimal difference between the performance of the solar modules occurs for the thickest c-Si absorber. When comparing the architectures from Figs. 1(e) to 1(b) and Figs. 1(f) to 1(d) in the case of 160 μm c-Si wafer, the difference in the annual EY goes down to 1.8 $\%_{rel}$ and 2.6 $\%_{rel}$, respectively. However, we stress that the pyramidal textures are challenging to apply for thinner wafers on which we concentrate here. Therefore, the considered nanodisk arrays constitute an excellent alternative because their fabrication is feasible, and they allow approaching the performance of the pyramidal textures.

Table 2. Comparison of the annual EY in Kansas City of the monofacial and bifacial solar modules with nanodisks and the solar modules with random pyramidal texture

Module architecture	Wafer thickness [μm]		
	40	80	160
	Energy yield [kWh·m^{-2}a^{-1}]		
Monofacial with nanodisks	337.7	348.7	358.1
Monofacial with random pyramidal texture	344.9	355.6	364.5
Bifacial with nanodisks	356.5	370.6	382.2
Bifacial with random pyramidal texture	366.6	380.6	392.0

Additionally, we considered the influence of albedo radiation for the module architectures (a)-(d) in Fig. 1. The results are shown in Fig. 7. Here, the annual EY of the four module architectures with a selected median c-Si absorber thickness of 40 μm is shown for the sandstone and grass ground surface compared to EY of the modules without albedo. Since the interfaces of the reference modules with standard ARC are flat, without albedo, the monofacial standard reference module outperforms the bifacial reference. While for the former, the backsheet reflects the light reaching it back into the cell, for the latter, a lot of light is lost due to transmittance when no LT structure is introduced. This difference is bigger with a smaller module tilt angle since less irradiation can hit the module from the back. However, as soon as albedo radiation is considered, the bifacial standard reference outperforms its monofacial counterpart. While for monofacial architecture albedo radiation does not make a significant difference, one can see a robust improvement in the annual EY for the bifacial case. The increase of the annual EY for the monofacial architecture varies depending on the module tilt and is stronger for locations with a greater θ_m (Anchorage). The relative improvement reaches up to around 0.8 $\%_{rel}$ with sandstone and 3.0 $\%_{rel}$ with grass as a ground surface for both the reference monofacial module with standard flat ARC and monofacial module with AR and LT nanodisk arrays with insignificant difference between them. In the case of the bifacial module architecture, a stronger increase of the annual EY is expected for the sunnier locations (Honolulu). It reaches up to 8.2 $\%_{rel}$ with sandstone, and 28.9 $\%_{rel}$ with grass ground surface in case of a reference bifacial module with standard flat ARC. For a bifacial module with AR and LT structures, the relative increase is 8.3 $\%_{rel}$ and 30.1 $\%_{rel}$ with sandstone and grass ground surface, respectively.
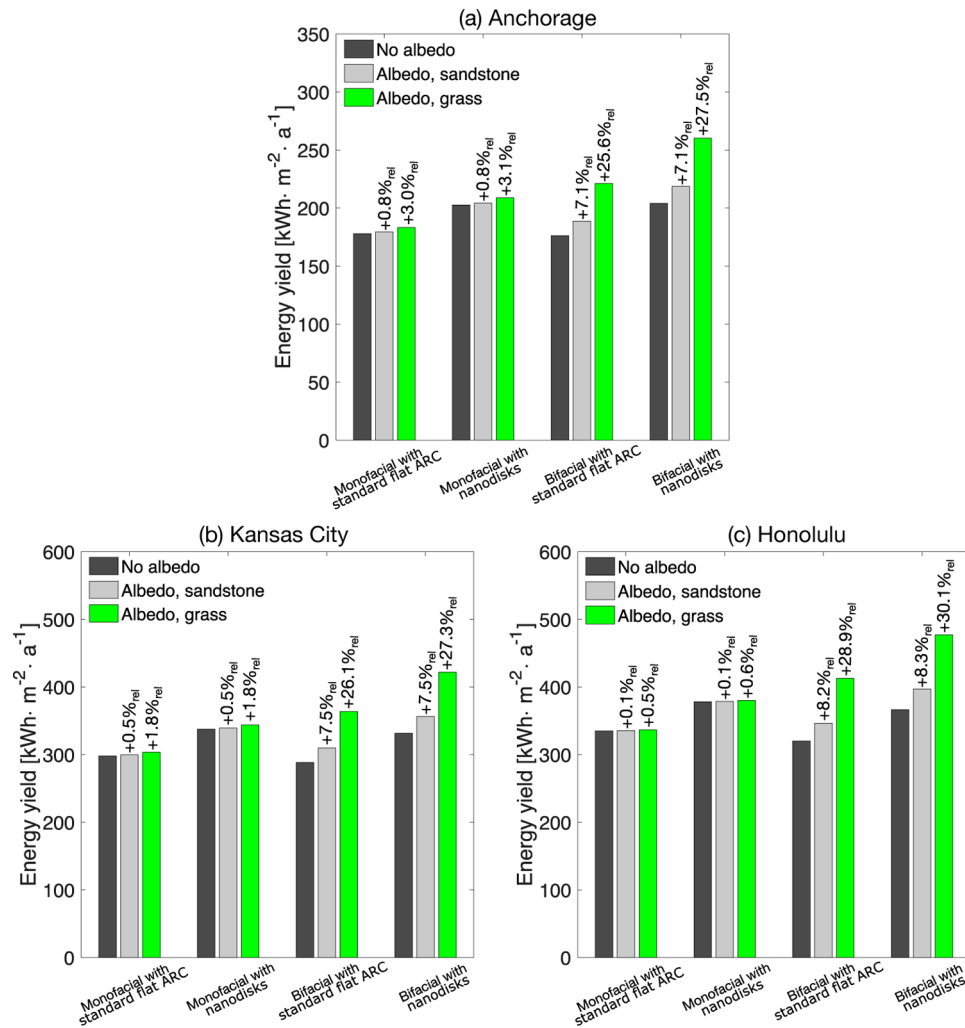
Fig. 7. Energy yield of the module architectures (a)-(d) from Fig. 1 for different locations when albedo irradiation is taken into account. For all solar module architectures, the c-Si absorber thickness was 40 μm.

4. Conclusions

We have numerically studied the annual energy yield (EY) under realistic irradiation conditions for monofacial and bifacial crystalline silicon (c-Si) heterojunction (HJT) solar module architectures with anti-reflective (AR) and light trapping (LT) titanium dioxide (TiO$_2$) nanodisk square arrays introduced on top of the front and rear ITO layers and compared their power outputs with the ones of the corresponding reference solar modules with standard flat ARCs. We have shown that while reducing the silicon absorber thickness down to 5 μm, the relative increase of the annual EY is reaching up to 23.3 %$_{rel}$ and 43.0 %$_{rel}$ for monofacial and bifacial modules with nanodisk coatings, respectively. This improvement is comparable for the locations with different climate conditions. Moreover, in the case of bifacial module architecture, taking into account the albedo radiation produces an additional boost of the module performance. Additionally, we compared the performance of the solar modules with nanodisk arrays to the state-of-the-art modules with random pyramidal texture. Even though the latter outperform the modules with the

nanodisks, the structures we propose prove to be a sufficiently good alternative for the silicon wafer thicknesses at which texturing becomes challenging.

The designed dielectric nanodisk arrays for the front and rear contacts of c-Si HJT solar cell have both a significant impact on the light absorption in the c-Si wafer. At the same time, their AR and LT properties are decoupled. The front AR nanodisk array has a relatively small individual disk size and lattice constant. The broadband backscattering suppression by the system with such AR nanodisks is related to the system's ability to preserve helicity (handedness) of the light for the illumination direction along the symmetry axis of the system. In contrast, the rear LT nanodisk array has larger features and array pitch and allows for efficient scattering into multiple scattering directions. Furthermore, these AR and LT nanodisk square array designs are not restricted to a specific material or a particular photovoltaic solar cell stack and, thus, can be investigated for different solar module configurations.

Disclosures. The authors declare no conflicts of interest.

Data availability. Data underlying the results presented in this paper are not publicly available at this time but may be obtained from the authors upon reasonable request.

References

1. K. Yoshikawa, H. Kawasaki, W. Yoshida, T. Irie, K. Konishi, K. Nakano, T. Uto, D. Adachi, M. Kanematsu, H. Uzu, and K. Yamamoto, "Silicon heterojunction solar cell with interdigitated back contacts for a photoconversion efficiency over 26%," Nat. Energy **2**(5), 17032 (2017).
2. W. Shockley and H. J. Queisser, "Detailed Balance Limit of Efficiency of p-n Junction Solar Cells," J. Appl. Phys. **32**(3), 510–519 (1961).
3. A. Richter, J. Benick, F. Feldmann, A. Fell, M. Hermle, and S. W. Glunz, "n-Type Si solar cells with passivating electron contact: Identifying sources for efficiency limitations by wafer thickness and resistivity variation," Sol. Energy Mater. Sol. Cells **173**, 96–105 (2017).
4. H. Seidel, L. Csepregi, A. Heuberger, and H. Baumgärtel, "Anisotropic Etching of Crystalline Silicon in Alkaline Solutions: I. Orientation Dependence and Behavior of Passivation Layers," J. Electrochem. Soc. **137**(11), 3612–3626 (1990).
5. K.-M. Han and J.-S. Yoo, "Wet-texturing process for a thin crystalline silicon solar cell at low cost with high efficiency," J. Korean Phys. Soc. **64**(8), 1132–1137 (2014).
6. X. Tan, W. Yan, Y. Tu, and C. Deng, "Small pyramidal textured ultrathin crystalline silicon solar cells with double-layer passivation," Opt. Express **25**(13), 14725–14731 (2017).
7. A. A. A. Omer, Z. He, S. Hong, Y. Chang, J. Yu, S. Li, W. Ma, W. Liu, W. El Kolaly, and R. Chen, "Ultra-thin silicon wafers fabrication and inverted pyramid texturing based on cu-catalyzed chemical etching," Silicon **13**(2), 351–359 (2021).
8. Z. Liu, S. E. Sofia, H. S. Laine, M. Woodhouse, S. Wieghold, I. M. Peters, and T. Buonassisi, "Revisiting thin silicon for photovoltaics: a technoeconomic perspective," Energy Environ. Sci. **13**(1), 12–23 (2020).
9. N. M. Haegel, H. Atwater, T. Barnes, C. Breyer, A. Burrell, Y.-M. Chiang, S. De Wolf, B. Dimmler, D. Feldman, S. Glunz, J. C. Goldschmidt, D. Hochschild, R. Inzunza, I. Kaizuka, B. Kroposki, S. Kurtz, S. Leu, R. Margolis, K. Matsubara, A. Metz, W. K. Metzger, M. Morjaria, S. Niki, S. Nowak, I. M. Peters, S. Philipps, T. Reindl, A. Richter, D. Rose, K. Sakurai, R. Schlatmann, M. Shikano, W. Sinke, R. Sinton, B. Stanbery, M. Topic, W. Tumas, Y. Ueda, J. van de Lagemaat, P. Verlinden, M. Vetter, E. Warren, M. Werner, M. Yamaguchi, and A. W. Bett, "Terawatt-scale photovoltaics: Transform global energy," Science **364**(6443), 836–838 (2019).
10. E. C. Garnett, B. Ehrler, A. Polman, and E. Alarcon-Llado, "Photonics for Photovoltaics: Advances and Opportunities," ACS Photonics **8**(1), 61–70 (2021).
11. M. A. Green and S. Pillai, "Harnessing plasmonics for solar cells," Nat. Photonics **6**(3), 130–132 (2012).
12. K. Catchpole and A. Polman, "Plasmonic solar cells," Opt. Express **16**(26), 21793–21800 (2008).
13. V. E. Ferry, L. A. Sweatlock, D. Pacifici, and H. A. Atwater, "Plasmonic nanostructure design for efficient light coupling into solar cells," Nano Lett. **8**(12), 4391–4397 (2008).

14. J. Hou, B. Yang, X. Li, C. Ma, B. Wang, H. Long, C. Yang, and S. Chen, "Efficient and stable thin-film crystalline silicon solar cell by introducing rotation factor in surface square pillar array grating," J. Nanophotonics **14**(01), 1 (2020).
15. J. He, Z. Yang, P. Liu, S. Wu, P. Gao, M. Wang, S. Zhou, X. Li, H. Cao, and J. Ye, "Enhanced Electro-Optical Properties of Nanocone/Nanopillar Dual-Structured Arrays for Ultrathin Silicon/Organic Hybrid Solar Cell Applications," Adv. Energy Mater. **6**(8), 1501793 (2016).
16. P. Spinelli, F. Lenzmann, A. Weeber, and A. Polman, "Effect of EVA Encapsulation on Antireflection Properties of Mie Nanoscatterers for c-Si Solar Cells," IEEE J. Photovoltaics **5**(2), 559–564 (2015).
17. S. Yalamanchili, E. Verlage, W.-H. Cheng, K. T. Fountaine, P. R. Jahelka, P. A. Kempler, R. Saive, N. S. Lewis, and H. A. Atwater, "High Broadband Light Transmission for Solar Fuels Production Using Dielectric Optical Waveguides in TiO2 Nanocone Arrays," Nano Lett. **20**(1), 502–508 (2020).
18. P. Spinelli, M. Verschuuren, and A. Polman, "Broadband omnidirectional antireflection coating based on subwavelength surface Mie resonators," Nat. Commun. **3**(1), 692 (2012).
19. J. Hou, W. Hong, X. Li, C. Yang, and S. Chen, "Biomimetic spiral grating for stable and highly efficient absorption in crystalline silicon thin-film solar cells," Opt. Express **25**(20), A922–A931 (2017).
20. K. X. Wang, Z. Yu, V. Liu, Y. Cui, and S. Fan, "Absorption Enhancement in Ultrathin Crystalline Silicon Solar Cells with Antireflection and Light-Trapping Nanocone Gratings," Nano Lett. **12**(3), 1616–1619 (2012).
21. O. Isabella, R. Vismara, D. Linssen, K. Wang, S. Fan, and M. Zeman, "Advanced light trapping scheme in decoupled front and rear textured thin-film silicon solar cells," Sol. Energy **162**, 344–356 (2018).
22. M. Singh, R. Santbergen, I. Syifai, A. Weeber, M. Zeman, and O. Isabella, "Comparing optical performance of a wide range of perovskite/silicon tandem architectures under real-world conditions," Nanophotonics **10**(8), 2043–2057 (2021).
23. M. T. Hörantner and H. J. Snaith, "Predicting and optimising the energy yield of perovskite-on-silicon tandem solar cells under real world conditions," Energy Environ. Sci. **10**(9), 1983–1993 (2017).
24. N. Tucher, O. Höhn, J. N. Murthy, J. C. Martinez, M. Steiner, A. Armbruster, E. Lorenz, B. Bläsi, and J. C. Goldschmidt, "Energy yield analysis of textured perovskite silicon tandem solar cells and modules," Opt. Express **27**(20), A1419–A1430 (2019).
25. J. Lehr, M. Langenhorst, R. Schmager, F. Gota, S. Kirner, U. Lemmer, B. S. Richards, C. Case, and U. W. Paetzold, "Energy yield of bifacial textured perovskite/silicon tandem photovoltaic modules," Sol. Energy Mater. Sol. Cells **208**, 110367 (2020).
26. F. Gota, M. Langenhorst, R. Schmager, J. Lehr, and U. W. Paetzold, "Energy yield advantages of three-terminal perovskite-silicon tandem photovoltaics," Joule **4**(11), 2387–2403 (2020).
27. M. Jošt, E. Köhnen, A. B. Morales-Vilches, B. Lipovšek, K. Jäger, B. Macco, A. Al-Ashouri, J. Krč, L. Korte, B. Rech, R. Schlatmann, M. Topič, B. Stannowski, and S. Albrecht, "Textured interfaces in monolithic perovskite/silicon tandem solar cells: advanced light management for improved efficiency and energy yield," Energy Environ. Sci. **11**(12), 3511–3523 (2018).
28. T. C. R. Russell, R. Saive, A. Augusto, S. G. Bowden, and H. A. Atwater, "The Influence of Spectral Albedo on Bifacial Solar Cells: A Theoretical and Experimental Study," IEEE J. Photovoltaics **7**(6), 1611–1618 (2017).
29. E. Slivina, A. Abass, D. Bätzner, B. Strahm, C. Rockstuhl, and I. Fernandez-Corbaton, "Insights into Backscattering Suppression in Solar Cells from the Helicity-Preservation Point of View," Phys. Rev. Appl. **12**(5), 054003 (2019).
30. C. Schinke, P. Christian Peest, J. Schmidt, R. Brendel, K. Bothe, M. R. Vogt, I. Kröger, S. Winter, A. Schirmacher, S. Lim, H. T. Nguyen, and D. MacDonald, "Uncertainty analysis for the coefficient of band-to-band absorption of crystalline silicon," AIP Adv. **5**(6), 067168 (2015).
31. "Filmetrics database, TiO2 Rutile," https://www.filmetrics.com/refractive-index-database.
32. Z. C. Holman, M. Filipic, A. Descoeudres, S. De Wolf, F. Smole, M. Topic, and C. Ballif, "Infrared light management in high-efficiency silicon heterojunction and rear-passivated solar cells," J. Appl. Phys. **113**(1), 013107 (2013).
33. Y. Jiang, S. Pillai, and M. A. Green, "Realistic Silver Optical Constants for Plasmonics," Sci. Rep. **6**(1), 1–7 (2016).
34. K. R. McIntosh, J. N. Cotsell, J. S. Cumpston, A. W. Norris, N. E. Powell, and B. M. Ketola, "An optical comparison of silicone and EVA encapsulants for conventional silicon PV modules: A ray-tracing study," in *2009 34th IEEE Photovoltaic Specialists Conference (PVSC)*, (IEEE, Philadelphia, PA, USA, 2009), pp. 000544–000549.
35. J. M. Siqueiros, R. Machorro, and L. E. Regalado, "Determination of the optical constants of MgF2 and ZnS from spectrophotometric measurements and the classical oscillator method," Appl. Opt. **27**(12), 2549–2553 (1988).
36. J. Pomplun, S. Burger, L. Zschiedrich, and F. Schmidt, "Adaptive finite element method for simulation of optical nano structures," Phys. Status Solidi B **244**(10), 3419–3434 (2007).
37. "EYcalc - energy yield calculator for multi-junction solar modules with realistic irradiance data and textured interfaces," https://github.com/PerovskitePV/EYcalc.
38. R. Schmager, M. Langenhorst, J. Lehr, U. Lemmer, B. S. Richards, and U. W. Paetzold, "Methodology of energy yield modelling of perovskite-based multi-junction photovoltaics," Opt. Express **27**(8), A507–A523 (2019).
39. K. Jäger, G. Köppel, M. Hammerschmidt, S. Burger, and C. Becker, "On accurate simulations of thin-film solar cells with a thick glass superstrate," Opt. Express **26**(2), A99–A107 (2018).
40. C. Gueymard, *SMARTS2: a simple model of the atmospheric radiative transfer of sunshine: algorithms and performance assessment* (Florida Solar Energy Center Cocoa, FL, 1995).

41. Z. C. Holman, A. Descoeudres, L. Barraud, F. Z. Fernandez, J. P. Seif, S. De Wolf, and C. Ballif, "Current Losses at the Front of Silicon Heterojunction Solar Cells," IEEE J. Photovoltaics **2**(1), 7–15 (2012).

42. M. C. Peel, B. L. Finlayson, and T. A. McMahon, "Updated world map of the Köppen-Geiger climate classification," Hydrol. Earth Syst. Sci. **11**(5), 1633–1644 (2007).